UC Berkeley

UC Berkeley Previously Published Works

Title

Single Particle Cathodoluminescence Spectroscopy with Sub-20 nm, Electron-Stable Phosphors

Permalink

Journal

ISSN

Authors

Swearer, Dayne F
Fischer, Stefan
Angell, Daniel K
et al.

Publication Date

DOI

Peer reviewed

Single particle cathodoluminescence spectroscopy with sub-20 nanometer, electron stable phosphors

Dayne F. Swearer[1] *, Stefan Fischer[1], Daniel K. Angell[1], Chris Siefe[1], A. Paul Alivisatos[2,3,4,5],

Steve Chu[6,7], Jennifer A. Dionne[1,8] *

[1]Department of Material Science and Engineering, Stanford University School of Engineering, Stanford, CA, 94305, USA

[2]Materials Science Division, Lawrence Berkeley National Laboratory Berkeley, CA, 94720, USA

[3]Department of Chemistry, University of California, Berkeley Berkeley, CA, 94720, USA

[4]Department of Materials Science and Engineering, University of California, Berkeley, Berkeley, CA, 94720, USA

[5]Kavli Energy Nanoscience Institute, Berkeley, CA, 94720, USA

[6]Department of Physics, Stanford University, Stanford, CA, 94305, USA

[7]Department of Molecular and Cellular Physiology, Stanford University, Stanford, CA, 94305, USA

[8]Department of Radiology, Stanford University School of Medicine, Stanford, CA, 94305, USA.

Abstract

Lanthanide-doped nanophosphors have emerged as promising optical labels for high-resolution, "multicolor" electron microscopy. Here, we develop a library of eleven unique lanthanide-doped nanophosphors with average edge lengths of 15.2 ± 2.0 nm (N = 4284). These nanophosphors consist of an electron stable $BaYF_5$ host lattice doped at 25% atomic concentration with the lanthanides Pr^{3+}, Nd^{3+}, Sm^{3+}, Eu^{3+}, Tb^{3+}, Dy^{3+}, Ce^{3+}, Ho^{3+}, Er^{3+}, Tm^{3+}, and Yb^{3+}. Under ~100 pA/nm^2 beam current in a transmission electron microscope, each nanophosphor species exhibits strong cathodoluminescence spectra with sharp characteristic emission lines for each lanthanide. The bright emission and stability of these nanoparticles enable not only ensemble, but also single-particle cathodoluminescence spectroscopy, which we demonstrate with $BaYF_5:Ln^{3+}$ where Ln^{3+} = Tb^{3+}, Ho^{3+}, Er^{3+}, Sm^{3+}, Eu^{3+}, or Pr^{3+}. Single-particle cathodoluminescence corresponds directly with HAADF intensity across nanoparticles, confirming high spatial localization of the measured cathodoluminescence signal of lanthanide-doped nanophosphors. Our synthesis and characterization of sub-20nm electron-stable nanophosphors provides a robust material platform to achieve single-molecule labeled correlative cathodoluminescence electron microscopy, a critical foundation for high-resolution correlation of single-molecules within the context of cellular ultrastructure.

Microscopy has a long history of enabling scientific breakthroughs in chemistry, materials science, and biology. Transmission electron microscopy (TEM) is one variation that has enabled remarkable advances in a wide range of imaging situations that span resolving the atomic structure in solid-state materials to identifying nanometer-scale features within cellular ultrastructures, albeit with the caveat that the TEM produces contrast-based images. To enhance image contrast, microscoscopists will often incorporate electron dense, molecule-specific labels such as immunogold to enhance image contrast for macromolecules of interest, but co-localization studies between two or more molecular targets remains challenging the black-and-white nature of contrast-based imaging techniques.[1,2] In juxtaposition, advances in optical microscopy have allowed for unprecedented chemical specificity through fluorescent labels; yet despite a myriad of advances in super-resolution techniques,[3–8] optical microscopy can still not rival the spatial resolution afforded by an electron microscope.

Recently, there has been significant effort to combine the distinct strengths of optical and electron microscopy into a unified imaging approach. Correlative light and electron microscopy has emerged as a technique to identify key macromolecules and proteins through spectrally distinguishable tags via optical microscopy and correlated high-resolution electron micrographs.[9] Differences in image resolution between the optical and electron imaging modalities has historically been a major obstacle, but recent developments in correlative super-resolution light and electron microscopy have begun to address the mismatch in resolution.[10] More decisively, inconsistencies in sample preparation and experimental workflows for each technique remains

the primary limiting factor in wide-spread adoption of this technique.[11–15] For example, fluorescence microscopy requires mild preparation conditions while sample preparation for electron microscopy requires strong chemical fixative agents that are known to have a detrimental effect on fluorescent probes. Furthermore, many correlated optical and electron microscopy techniques are performed in sequential imaging steps that can introduce inhomogeneous damage and complicate image correlation.

In order to overcome the challenges of correlated optical and electron microscopy, techniques have emerged that combine simultaneous spatial and spectral imaging of a sample, taking advantage of electron-beam induced optical emission (cathodoluminescence; CL) from samples labeled with spectroscopically identifiable tags.[15,16] Simultaneous electron microscopy and cathodoluminescence spectroscopy (EM-CL) can be adapted to both scanning electron microscopes (SEMs)[13,17,18] and transmission electron microscopes (TEMs)[19] as long as the proper hardware for CL collection is present. Advantageously, CL is localized, enabling spectral information to be acquired with nanometer spatial resolution with simultaneous acquisition of information about sample morphology, cellular ultrastructural features, and composition. Emerging methods for time-resolved CL detection could allow for further differentiation of cathodoluminescence labels and remove background autofluorescence.

Maturation and wide-spread adoption of EM-CL as an imaging technique still faces several distinctive challenges.[20] Of utmost importance is the development of bright and stable nanophosphors to enable single biomolecule labeling and localization.[20] In recent years, lanthanide-doped nanoparticles have emerged as promising candidates for cathodoluminescent nanophosphors. Organic fluorophores or fluorescent proteins, commonly employed in

fluorescence microscopy, undergo radiolysis and rapidly degrade under electron irradiation.[21] Solid-state alternatives, such as quantum dots, bleach and blink under electron irradiation and are non-viable for extended imaging studies.[22–24] Lanthanide-doped nanophosphors are spectrally tunable based on lanthanide identity, have shown high cytocompatibility[25], and have versatile surface functionalization chemistry for molecular targeting applications.[26] Here, we present a robust material platform for small, bright, and stable nanophosphors for EM-CL. This contribution provides a foundation for multiplexed molecular labeling.

Results and Discussion

We have developed a nanophosphor library of small (sub-20 nm), electron-beam stable, lanthanide-doped nanophosphors based on an alkaline-earth rare-earth fluoride ($M_{1-x}Ln_xF_{2+x}$; MLnF) host lattice with unique spectroscopic fingerprints measured at the single-particle level. We have previously shown that solvothermal decomposition of alkaline-earth and rare-earth trifluoroacetates (TFA) can produce several distinct MLnF host lattices that are efficient for infrared-to-visible upconversion when doped with Yb^{3+} and Er^{3+} and have been systematically and extensively characterized with XRD and ICP-OES.[27,28] In this study, the $BaYF_5$ host lattice was selected due to its increased resistance to knock-on damage when compared to other sodium rare-earth fluoride host-lattice alternatives.[29] Briefly, solvothermal decomposition of salts of Ba^{2+}-TFA, Y^{3+}-TFA, and Ln^{3+}-TFA in a mixture of octadecene, oleic acid, and oleylamine at 300 ºC was used to produce 4.5 ± 0.6 nm (N = 2031) seeds. These seeds were subject to two subsequent shelling procedures to produce the final cubic nanophosphors with edge-lengths of 15.2 ± 2.0 nm (N = 4284). A scheme detailing the synthetic procedure is shown in Figure 1A, and average nanoparticle sizes are presented in Figure 1B. Representative bright-field

transmission electron micrographs (TEM) and detailed size statistics histograms of $BaYF_5:Ln^{3+}$

seeds (Fig. S1) and nanophosphors (Fig. S2) used in this study can be found in the supporting

information (SI) along with more detailed synthetic procedures. For the nanophosphors studied

here, Y^{3+} cations were replaced at 25% with one-of-eleven lanthanide ions (where $Ln^{3+} = Pr^{3+}$,

Nd^{3+}, Sm^{3+}, Eu^{3+}, Tb^{3+}, Dy^{3+}, Ce^{3+}, Ho^{3+}, Er^{3+}, Tm^{3+}, Yb^{3+}). The unit cell of $BaYF_5:Ln^{3+}$ is shown

in Figure 1B along the (0 0 1) and (0 1 0) Miller indices, where the Y^{3+} ion (dark green) has been

replaced by a Ln^{3+} ion (magenta) although in the $BaYF_5$ host lattice the lanthanide dopant may

replace either Ba^{2+} or Y^{3+} site.[24] Representative TEMs of $BaYF_5:Sm^{3+}$ seeds and final

nanophosphors are shown in Figure 1D and Figure 1E, respectively. A high-resolution TEM of

an ~12 nm $BaYF_5:Sm^{3+}$ nanophosphor after the first growing procedure is shown in Figure 1F.

Nanoparticle stability under the electron beam was verified by measuring panchromatic

photon counts (Figure S3). The stability of ensemble measurements shows a ~50% decrease over

8 minutes of continuous irradiation, and single particle stability exhibited an ~30% decrease over

two minutes under ~100 pA/nm^2 beam current. Loss of emission intensity for lanthanide-doped

nanophosphors is well known to occur via knock-on damage.[29] Compared to a previous report[30]

by Keevend et al. on beam stability of other commonly used phosphors, such as the organic

fluorophore 4′-6-diamidino-2-phenyl-indole (DAPI), semiconductor quantum dots (CdTe and

CdSe/CdS), and two types of lanthanide-doped nanocrystals ($Y_2O_3:Tb^{3+}$ and $YVO_4:Bi^{3+}Eu^{3+}$), the

$BaYF_5:Ln^{3+}$ nanophosphors presented here exhibit greater beam stability over two minutes of

continuous electron bombardment. DAPI and semiconductor quantum dots lost ~80% of their

CL emission over 120 seconds.[30] Organic fluorophores are well-known to experience structural

damage under electron beams.[31] $Y_2O_3:Tb^{3+}$ and $YVO_4:Bi^{3+}Eu^{3+}$ sustained ~60% of the emission

over 120 seconds[30], but previous report by Furukawa et al. on similar phosphors (Y_2O_3:Eu^{3+}) demonstrated up to 97% sustained CL emission over 60 seconds.[18] Our system exhibits ~70% sustained CL emission under electron bombardment at 80 kV and ~100 pA/nm^2, but we stress that nanophosphors properties are highly dependent on specific conditions of the material composition, nanoparticle size, and microscope conditions, particularly beam and vacuum settings.
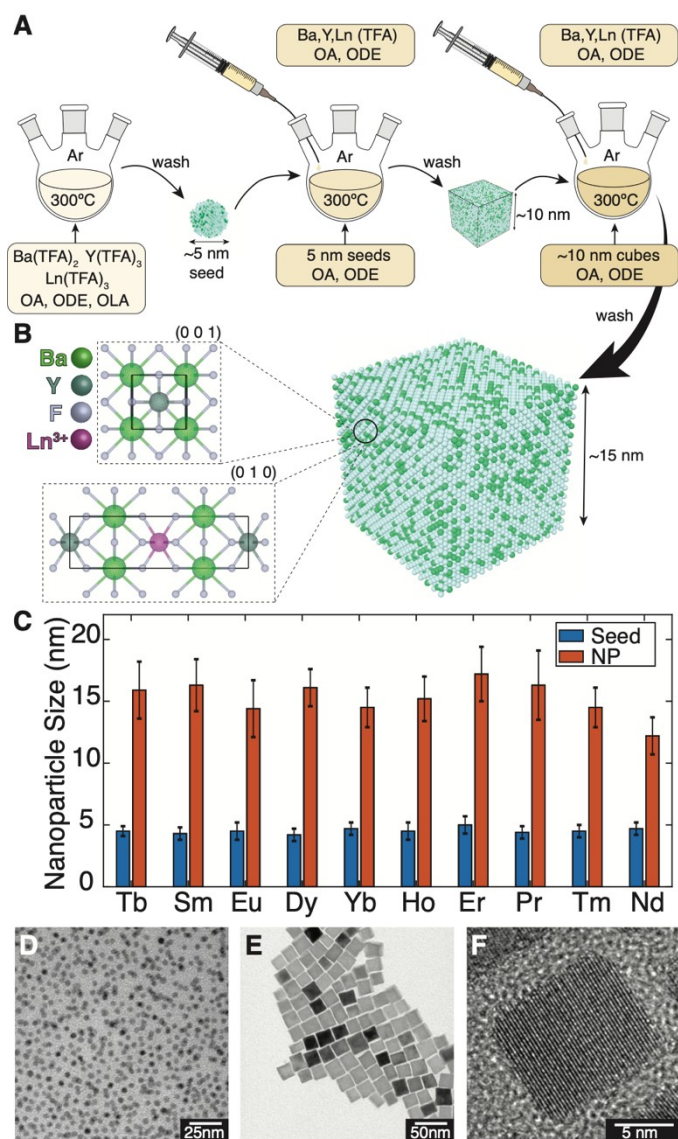
Figure 1. **Synthesis of Lanthanide-doped BaYF₅ nanophosphors.** (A) Schematic of the three-step synthetic procedure for preparation of $BaYF_5:Ln^{3+}$ where the final product are cubic nanocrystals with average edge lengths of 15.2 ± 2.0 nm. Acronyms used here refer to oleic acid (OA), octadecene (ODE), oleylamine (OLA), and trifluoroacetate (TFA). (B) Crystal structure of a $BaYF_5:Ln^{3+}$ unit cell oriented normal to the (0 0 1) and (0 1 0) Miller indices on top and bottom, respectively. This representative structure was obtained from a publicly available crystallographic information file from the Materials Project.[32] (C) Representative size statistics of $BaYF_5:Ln^{3+}$ seeds and nanophosphors (NP); further size histograms and representative TEM images of each sample are shown in Figs. S1 and S2. (D) A representative bright-field transmission electron micrograph of ~5 nm $BaYF_5:Sm^{3+}$ seeds after the first step in the synthetic procedure outlined in (A). (E) A representative bright-field transmission electron

micrograph of $BaYF_5:Sm^{3+}$ nanophosphors after two subsequent growing procedures. (F) High-resolution transmission electron micrograph of a single $BaYF_5:Sm^{3+}$ nanophosphor after the first growing procedure.

CL spectra were acquired within a (scanning) transmission electron microscope ((S)TEM; FEI Titan) operating at 80 kV (see Figure 2A).[33] Upon excitation with the electron beam, two concave mirrors on the top and bottom of the sample collected CL and focused it into two optical fibers. The CL signal is then carried through the fiber optics to either a photomultiplier tube (PMT) or charge coupled device (CCD) for detection; an optics diagram for the CL collection system is provided in Figure S4.

For all CL spectra, nanoparticles were drop-cast onto ultrathin carbon TEM grids. When exposed to an incident electron beam, several measurable signals are generated from the sample (Figure 2B). Collection of visible light emission (CL) is the main focus in this work. However, in addition, reliable spatial information is obtained from transmitted electrons that are elastically scattered, forming the basis for high-angle annular dark field (HAADF) images. Characteristic X-rays and inelastically scattered transmitted electrons may also be utilized to cross reference material composition using energy dispersive X-ray spectroscopy or electron energy loss spectroscopy (EELS), respectively.

Ensemble CL spectra of $BaYF_5:Ln^{3+}$ nanoparticles were collected using STEM-CL at 80kx magnification and ~100 pA/nm^2 beam current by scanning the focused electron beam over a wide-field area of nanophosphor aggregates, estimated to contain between 10^3 - 10^4 individual nanoparticles for 120 seconds. The ensemble CL spectra in Figure 2C show distinct spectral fingerprints for each Ln^{3+} dopant. Eight nanophosphors predominantly exhibit characteristic CL emission within the visible (400 – 700 nm) portion of the electromagnetic spectrum (Ln^{3+} =

Sm^{3+}, Er^{3+}, Eu^{3+}, Dy^{3+}, Ho^{3+}, Tb^{3+}, Tm^{3+}, and Pr^{3+}) while two nanophosphors luminesce almost exclusively within the near-IR (Ln^{3+} = Yb^{3+} and Nd^{3+}). An ensemble spectrum for $BaYF_5$:Ce^{3+} was also acquired but produced a broad non-specific emission profile spanning the visible due to higher prevalence of *f-d* transitions (Figure S5).[34] The distinct CL spectra for each of the ten lanthanide dopants hosted within $BaYF_5$ suggests these materials are a unique material platform with potential as uniquely identifiable optical nanoprobes. The maximum emission wavelengths and transition assignments for each nanophosphor are summarized in Table S1.
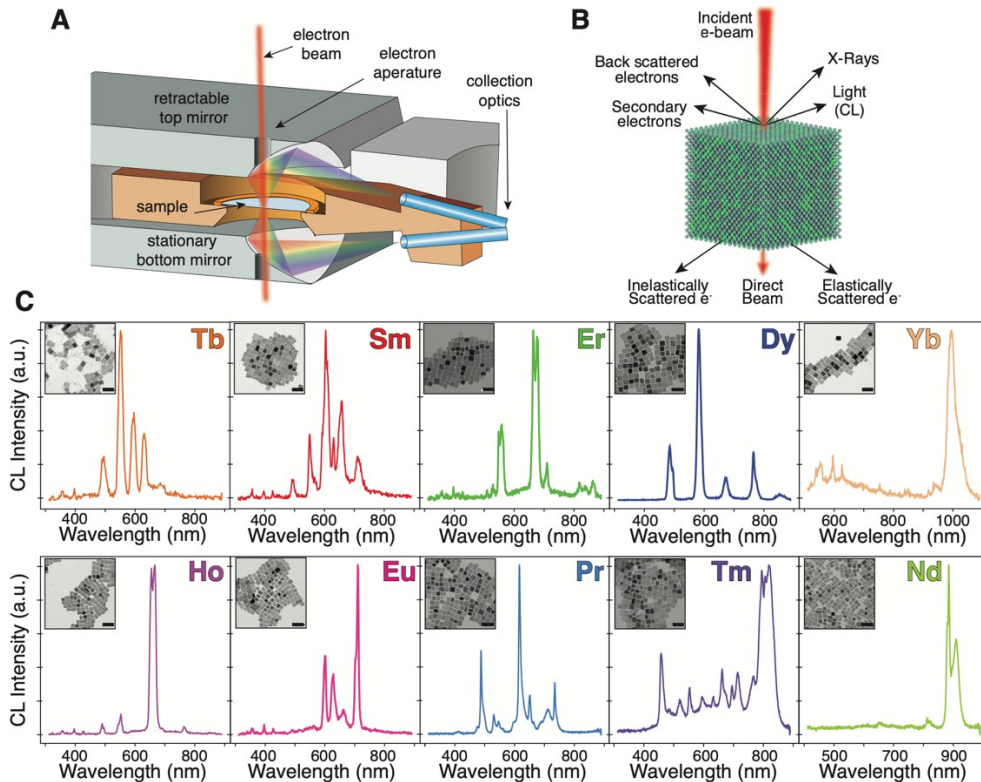

Figure 2. Ensemble Cathodoluminescence Characterization. (A) Illustrative representations of the Vulcan cathodoluminescence (CL) holder that enables for collection of CL signals within the TEM (top) representation of the holder and (bottom) a cross sectional view showing optical emission (CL) collection from two parabolic mirrors. (B) Schematic showing an example of different types of measurable signals that are generated when an electron

beam is incident on lanthanide-doped nanophosphors; cathodoluminescence is one of several possible signals from lanthanide-doped nanophosphors. Secondary and back-scattered electrons are collected in SEM based experiments, while all other signals are collected in the TEM. (C) Ensemble CL spectra for ten varieties of $BaYF_5:Ln^{3+}$; the identity of the lanthanide doped into the host lattice is positioned in the top right corner of each spectra. Insets show a representative transmission electron micrograph for each sample; all scale bars are 25 nm.

In order for lanthanide-doped nanophosphors to be effective optical labels, they must be sufficiently bright to produce spectroscopically distinct signatures at the single particle level; our $BaYF_5:Ln^{3+}$ nanoparticles meet these criteria. Single particle CL spectra for $BaYF_5:Ln^{3+}$ (where $Ln^{3+} = Tb^{3+}$, Ho^{3+}, Sm^{3+}, Er^{3+}, Eu^{3+}, Pr^{3+}, and Sm^{3+}) are shown in Figure 3. Single particle spectra were acquired as 30-second single frame integrations, using a ~1nm STEM probe on isolated nanoparticles. Generally, single-particle and ensemble CL spectra of lanthanide-doped nanophosphors match well with regards to the emission maxima of distinct lines and their relative intensities. The single particle CL spectrum for $BaYF_5:Tb^{3+}$ was consistent with the four distinct lines discussed in the ensemble spectrum and the $^5D_4 \rightarrow {}^7F_4$ transition remained the most intense transition in all measurements.[35] In contrast to the $BaYF_5:Sm^{3+}$ ensemble spectra, the single particle spectrum of $BaYF_5:Sm^{3+}$ is defined by three strong luminescent lines centered at 568, 608, and 656 nm corresponding to the $^4G_{5/2} \rightarrow {}^6H_{5/2}$, $^6H_{7/2}$, and $^6H_{9/2}$ transitions, respectively.[36] The absence of the $^4G_{5/2} \rightarrow {}^6H_{11/2}$ and $^4G_{7/2} \rightarrow {}^6H_{5/2}$ transition are not unexpected due to their relatively low intensity even in the ensemble spectrum. The single particle spectrum for $BaYF_5:Er^{3+}$ displayed two main lines centered at 672 and 553 nm; fine splitting in the ensemble spectra is not observed in the single particle spectra due to spectral binning in single-particle spectra acquisition.[37] The single particle spectrum of $BaYF_5:Ho^{3+}$ is dominated by a main emission at 660 nm arising from $^5F_5 \rightarrow {}^5I_8$ transition.[38] The single particle spectrum from

BaYF$_5$:Eu^{3+} was the weakest of those acquired during the course of this study, yet the $^5D_0 \rightarrow$ $^7F_4$ centered at 705 nm and $^5D_0 \rightarrow$ $^7F_1$ centered at 600 nm are observable in the single particle spectrum.[39] Previous reports on Eu-doped ceramics have more frequently reported the $^5D_0 \rightarrow$ $^7F_2$ transition to be of highest intensity in the CL spectrum, suggesting BaYF$_5$ lattices may promote select quantum transitions not seen in other ceramic hosts such as Y$_2$O$_3$ or TiO$_2$.[40] For BaYF$_5$:Pr^{3+} the ensemble and single particle spectra were identical with maximum emission occurring at 615 nm corresponding to the $^1D_2 \rightarrow$ $^3H_4$ transition.[41] Generally, single-particle and ensemble CL spectra of lanthanide-doped nanophosphors match well with regards to the emission maxima of distinct lines and their relative intensities. However, some weaker transitions and fine-splitting features were lost at the single particle level due to reduced signal-to-noise.

Using BaYF$_5$:Tb^{3+} (nominally doped at 25% Tb^{3+}) as a model system, we found that, on a single-particle level, variability in the total integrated photon counts at 543 nm over a 30 second acquisition ranged from 225 – 425 counts per second. We also found that CL intensity does not strongly correlate with nanoparticle edge length (Fig. S6a). Therefore, CL count variability is likely a result of variation in doping concentrations between individual nanoparticles (Figure S6b). Assuming a collection efficiency of 50%[42], we estimate that for the single particle spectrum of Eu^{3+} doped nanophosphors, which had the lowest signal-to-noise ratio of those nanophosphors whose single-particle spectra were experimentally realized, result from the detection of ~200 photons/second from a single nanoparticle, and currently represents a current lower bound for detectability. The realization of single-particle spectra with detection limits as low as 200 photons per second from a single nanoparticle is promising for the potential of these lanthanide-doped nanophosphors as sensitive and spectroscopically unique probes. Integrating more sensitive collection optics could lower this detection limit in the future experiments.

While point spectra of single nanoparticles are important for recognizing lanthanide-doped nanophosphors, it is also important to understand spatial resolution for large-area scans. CL imaging allows for sub-diffraction imaging by exploiting the electron beam as an optical excitation source. Previous work on Ag nanocubes using coherent cathodoluminescence super-resolution microscopy revealed that the intensity of CL and secondary electron emission varied spatially due to exponentially decaying tails of evanescent coupling of the electron beam to the local density of optical states.[43] Depending on the accelerating voltages used, the CL decay lengths could be detected up to 12 nm away from the physical edge of the Ag nanocube.[43] In metals, like Ag nanocubes, coherent CL dominates because incoherent CL is suppressed by non-radiative channels.[33] However, the primary CL channel in many wide-band gap semiconductors, and the $BaYF_5:Ln^{3+}$ nanophosphosphors in our study, is incoherent CL that results from the generation of a bulk plasmon and direct radiative electron-hole recombination and scattering into defect color centers (*i.e.,* trivalent lanthanide dopants) for emission.[44,45] A low-loss EELS spectra of $BaYF_5:Tb^{3+}$ is included as Fig. S9, but is convoluted by $O_{2,3}$ core-losses of Ba, Y, and Tb making specific determination of the bulk plasmon challenging. The 15.2 ± 2.0 nm edge length particles presented here may represent the smallest total volume nanoparticles observed with STEM-CL measurements, however previous work by Jacobsohn et al. has shown scintillation under X-ray and ^{241}Am irradiation in rare-earth doped fluoride nanoparticles (i.e., CaF:Eu and $BaF_2:Eu$) in sizes as small as ~4 nm.[46]

The use of ceramic host lattices allows for reduction in the CL decay length to the physical edge of the nanophosphor. To study the spatial extent of the CL response in lanthanide-doped nanophosphors, the electron beam was scanned over three $BaYF_5:Tb^{3+}$ nanophosphors with 0.5 nm steps (Figure 3B) and a PMT was used to collect panchromatic images to maximize

signal-to-noise. Rapid CL onset and offset correspond directly with HAADF intensity across all three nanoparticles confirming high spatial localization of the measured STEM-CL of lanthanide-doped nanophosphors. The CL emission from $BaYF_5:Tb^{3+}$ nanophosphors was bandpass filtered at 546 ± 10 nm to show a similar trend in the spatial resolution within a narrow spectral window, albeit with slightly longer acquisition times and larger step sizes (2.5 nm). The rapid onset of CL in both spectrally filtered and unfiltered CL imaging reinforces the potential of $BaYF_5:Ln^{3+}$ nanophosphors for high-resolution luminescent markers because to the near-zero decay lengths associated with incoherent CL from these $BaYF_5:Ln^{3+}$ nanophosphors.

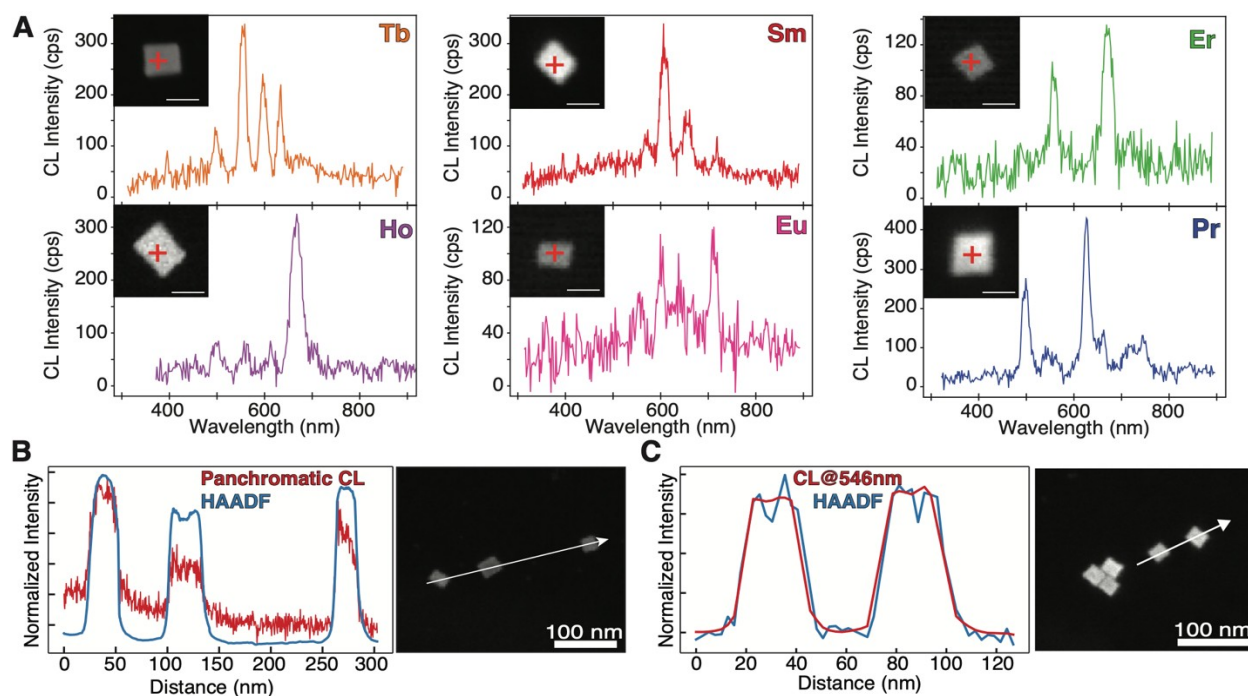Figure 3. **Single Particle Cathodoluminescence.** (A) Single particle spectra for $BaYF_5:Ln^{3+}$ where Ln = Tb^{3+}, Ho^{3+}, Er^{3+}. Sm^{3+}, Eu^{3+}, and Pr^{3+}. Each spectrum was collected by focusing a STEM probe with a beam current of ~100 pA/ nm^2 and a beam size of ~1nm into the center of a single nanophosphor during a 30 second acquisition. Inset shows a representative single particle. The red '+' corresponds to the parked position of the electron beam during spectral acquisition; scale bars are 25 nm. (B) Panchromatic CL imaging acquired at 0.5 nm step sizes across three spatially separated $BaYF_5:Tb^{3+}$ nanophosphors. Rapid onset of CL and HAADF signals demonstrate the high spatial

resolution afforded using STEM-CL. (C) Band-pass filtered panchromatic CL line scans across two BaYF$_5$:Tb^{3+} nanophosphors at 2.5 nm step-sizes.

In addition to the development of small, bright, and stable nanophosphors, multiplexed imaging (*i.e.,* differentiating two or more lanthanide-doped nanophosphors based on their optical signatures) is an critical milestone required of cathodoluminescent nanoprobes for EM-CL. This is important for practical future applications because it will allow for the high-resolution identification of multiple molecules within a sample. As one example. there is significant evidence that immunological responses can be complex orchestrations between the interactions of multiple intra- and intercellular protein interactions.[47,48] Therefore, the simultaneous identification of multiple labeled membrane proteins is an important step to imaging and mapping single molecules in the context of cellular ultrastructure.

We considered mixed samples of BaYF$_5$:Tb^{3+} and BaYF$_5$:Ho^{3+} deposited onto a carbon grid; these phosphors were selected due to the minimal overlap of their primary emission wavelengths and robust single-particle CL intensity. Simultaneously acquired HAADF, core-loss EELS, and panchromatic CL images were used to correlate the spatial origins of the CL signals with elemental identities resolved with EELS (Figure 4). From the wide-field HAADF image (Figure 4A), a subsection scan produced a correlative HAADF-EELS spectrum image (Figure 4B) containing a representative aggregate of Tb^{3+} and Ho^{3+} doped BaYF$_5$ nanophosphors. The spectrum image in Figure 4C, D were background subtracted and integrated over a 10eV window at 1241 and 1351 eV to map the relative loss probability of Tb-M$_5$ and Ho-M$_5$ edges, respectively. Core-loss EELS mapping of elemental distributions of Tb^{3+} (Figure 4C) and Ho^{3+} (Figure 4D) reveal distinctive mixing of BaYF$_5$:Tb^{3+} and BaYF$_5$:Ho^{3+} nanoparticles,

indistinguishable by HAADF contrast alone. Simultaneous acquisition of band-pass filtered panchromatic CL images over the same region of interest at 546 ± 10 nm (corresponding to Tb^{3+} $^5D_4 \rightarrow \,^7F_5$ transition; Figure 4E) and at 647 ± 10 nm (corresponding to $Ho^{3+}\, ^5F_5 \rightarrow \,^5I_8$ transition; Figure 4F), however, revealed no distinguishable spatial resolution for the filtered panchromatic CL images.

The lack of spatially resolvable CL based on lanthanide identity likely arises from a combination of competing effects that introduce delocalization to CL acquisition. Many of these effects were presented systematically by Zagonel *et al*. in an alternating GaN/AlN quantum disk heterostructure.[49] In semiconductors the electric field created by a fast moving electron beam can cause bulk and surface excitations through Coulombic coupling. These excitations result in electron-hole pair generation that can either radiatively recombine at the band edge, resulting in photon emission with energies equal to or greater than the material bandgap (E_g of $BaYF_5$ is ~6.45 eV)[32] or scatter off of defects promoting the excitation of color centers (*i.e.,* trivalent lanthanide dopants). The possibility of UV photon emission followed by parasitic absorption at defect color centers in nearby nanocrystals seems plausible based upon our experimental observations and cannot be ruled out. However, an additional source of delocalization could be secondary electron enhancement of the CL signal.[50] Electron hole-pairs typically have diffusion lengths on the order of 100 nm in ionic crystals[46], much larger than the physical size of the nanophosphors in this study. Therefore, any electrons that reach the nanophosphor surface prior to radiative or non radiative recombination have a probability to escape into the vacuum where they may travel several hundred microns before arriving at, and exciting, subsequently nanophosphors through parasitic CL absorption.[51] When CL spectra were collected on mixed $BaYF_5:Tb^{3+}$ and $BaYF_5:Ho^{3+}$ samples, the resulting spectra were convoluted by contributions

from both Tb^{3+} and Ho^{3+} (Figure S7). The most likely cause of this spectral mixing is due to the generation of secondary electrons when materials interact with the electron beam. We verified that secondary electrons can enhance CL signal from $BaYF_5$:Tb^{3+} nanophosphors by collecting ensemble CL spectra when the electron beam was illuminated over the carbon-supported nanophosphors and when the electron beam was focused on the edge of the copper-grid and found a ~3.5x enhancement of total counts during indirect secondary electron excitation (Fig. S8). In future work, given the variability of particle-to-particle CL emission intensity of key *4f-4f* transitions (Figure S6) deconvolution of mixed-CL signals will require extensive investigations into the role of single-particle lanthanide-doping density on quantitative CL emission. It may also be possible in the future to extend modern analytic tools such as machine learning based approaches to deconvolute complex CL spectra.[52]

While the data presented here demonstrates that EELS is a viable analytical technique to identify lanthanide-doped nanophosphors through core-loss measurements, CL still maintains several key advantages as a platform for future work. First, CL measurements can identify specific optical fingerprints that can readily be measured in additional correlative measurements (e.g. photoluminescence and optical microscopy). Second, trivalent lanthanides, due to their long-lived and spin-forbidden *4f-4f* transitions, produce optical emissions on timescales on the order of several hundred microseconds or even milliseconds, which may be uniquely probed in the future with time-resolved CL measurements. These emission lifetimes are much longer than cellular autofluorescence, which may be key to identifying individual nanophosphors in future biolabeling experiments. And finally, CL measurements are more easily adapted to different electron microscopy tools such as STEM, demonstrated here, and SEM demonstrated

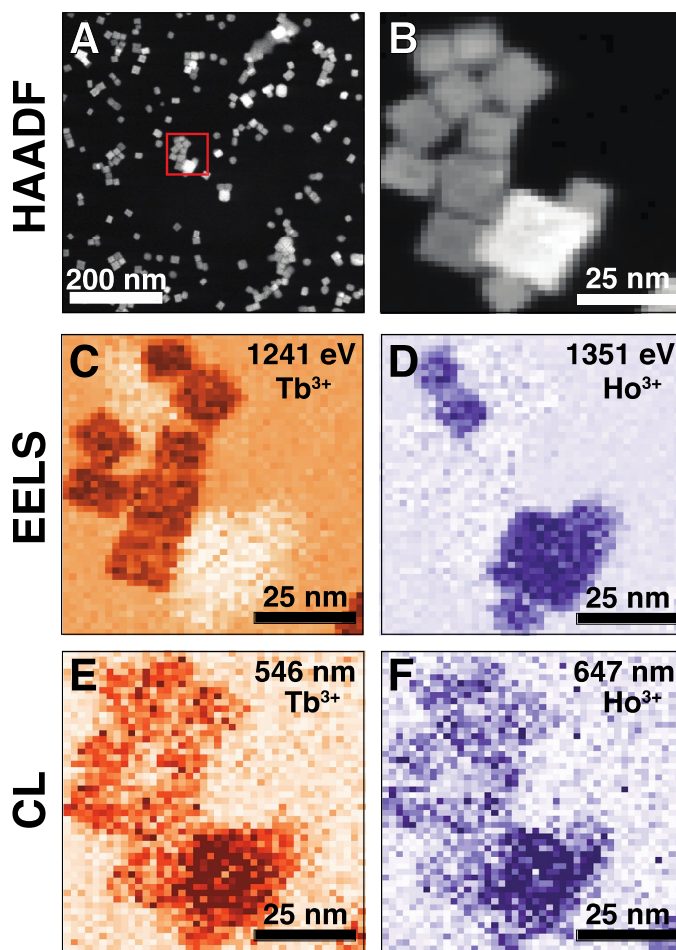previously.[16] These advantages position CL as an important tool for electron microscopy in the future.

Figure 4. **Correlated panchromatic cathodoluminescence imaging and electron energy loss spectroscopy on a mixed BaYF$_5$:Ho^{3+} and BaYF$_5$:Tb^{3+} nanophosphor systems**. (A) Wide-field HAADF image of a mixed Tb^{3+}/Ho^{3+} sample, where no visible difference between material composition can be observed. The region of interest for correlative EELS/CL measurements is marked with a red square. (B) HAADF spectrum image of the region of interest showing nanophosphor size and spatial distribution. (C) Background subtracted EELS maps corresponding to spectral integration starting at 1241 eV over a 10eV window corresponding to the Tb-M$_5$ edge. BaYF$_5$:Tb^{3+} are highlighted in orange. (D) Background subtracted EELS maps corresponding to spectral integration starting at 1351

eV over a 10eV window corresponding to the Ho-M_5 edge. (E) Band-pass filtered panchromatic CL at 546 ± 10 nm corresponding to the Tb^{3+} $^5D_4$ → $^7F_5$ transition. (F) Band-pass filtered panchromatic CL at 657 ± 10 nm corresponding to the Ho^{3+} $^5F_5$ → $^5I_8$ transition.

Conclusion

We have introduced lanthanide-doped alkaline-earth rare-earth fluorides as a new platform for cathodoluminescent nanophosphors with sufficient stability under ~100 pA/nm² of 80 kV electron beam for collection of single-particle spectra. Through a solvothermal decomposition approach, we have demonstrated how a library of ten nanophosphor varieties each with unique ensemble optical signatures can be synthesized. We have demonstrated that these nanophosphors are sufficiently stable and bright enough to enable the collection of single-particle CL spectra with average edge lengths of 15.2 ± 2.0 nm. In addition to addressing the urgent need to develop bright and stable cathodoluminescent nanophosphors[20], we also explored the feasibility of our nanophosphor library for multiplexed spectral imaging. These experiments revealed that even at the single-particle level, band-pass filtered panchromatic CL images and CL spectra suffer from signal convolution by nearby nanophosphors. We anticipate that the challenge associated with multiplexed CL imaging will be overcome with future work in new analytic methods for spectral deconvolution of mixed-lanthanide CL systems in combination with systematic studies on the influence of lanthanide-doping on a single-particle basis. These nanophosphors represent a promising nanophotonic material platform that could replace immunogold labeling in single-molecule tagging to go beyond contrast-based imaging and into the realm of color electron microscopy of physical and biological samples. The advances

presented here embody a key development in realizing bright and stable probes for future applications in correlative cathodoluminescence electron microscopy.

ASSOCIATED CONTENT

Supporting Information.

This material is available free of charge via the internet at http://pubs.acs.org. The supporting information includes additional details on materials and methods, Figures S1–S10, and Table S1 (PDF).

AUTHOR INFORMATION

Corresponding Author

*dayne@stanford.edu * jdionne@stanford.edu

Author Contributions

D.F.S., S.F., J.A.D. developed the study. D.F.S. and S.F. synthesized the lanthanide doped nanophosphors. D.F.S., S.F., and D.K.A. collected and processed the CL data. C.S. developed the nanoparticle sizing algorithm and performed nanoparticle size-statistics. The manuscript was

written through contributions of all authors. All authors have given approval to the final version of the manuscript.

References

(1)   Gopal, S.; Chiappini, C.; Armstrong, J. P. K.; Chen, Q.; Serio, A.; Hsu, C. C.; Meinert, C.; Klein, T. J.; Hutmacher, D. W.; Rothery, S.; Stevens, M. M. Immunogold FIB-SEM: Combining Volumetric Ultrastructure Visualization with 3D Biomolecular Analysis to Dissect Cell–Environment Interactions. *Adv. Mater.* **2019**, *31* (32). https://doi.org/10.1002/adma.201900488.

(2)   Melo, R. C. N.; Morgan, E.; Monahan-Earley, R.; Dvorak, A. M.; Weller, P. F. Pre-Embedding Immunogold Labeling to Optimize Protein Localization at Subcellular Compartments and Membrane Microdomains of Leukocytes. *Nat. Protoc.* **2014**, *9* (10), 2382–2394. https://doi.org/10.1038/nprot.2014.163.

(3)   Hell, S. W.; Wichmann, J. Breaking the Diffraction Resolution Limit by Stimulated

        Emission: Stimulated-Emission-Depletion Fluorescence Microscopy. *Opt. Lett.* **1994**, *19*

        (11), 780. https://doi.org/10.1364/ol.19.000780.

(4)   Balzarotti, F.; Eilers, Y.; Gwosch, K. C.; Gynnå, A. H.; Westphal, V.; Stefani, F. D.; Elf,

        J.; Hell, S. W. Nanometer Resolution Imaging and Tracking of Fluorescent Molecules

        with Minimal Photon Fluxes. *Science* **2017**, *355*, 606–612.

        https://doi.org/10.1126/science.aak9913.

(5)   Klar, T. A.; Jakobs, S.; Dyba, M.; Egner, A.; Hell, S. W. Fluorescence Microscopy with

        Diffraction Resolution Barrier Broken by Stimulated Emission. *Proc. Natl. Acad. Sci. U.

        S. A.* **2000**, *97* (15), 8206–8210. https://doi.org/10.1073/pnas.97.15.8206.

(6)   Betzig, E.; Patterson, G. H.; Sougrat, R.; Lindwasser, O. W.; Olenych, S.; Bonifacino, J.

        S.; Davidson, M. W.; Lippincott-Schwartz, J.; Hess, H. F. Imaging Intracellular

        Fluorescent Proteins at Nanometer Resolution. *Science* **2006**, *313* (5793), 1642–1645.

        https://doi.org/10.1126/science.1127344.

(7)   Rust, M. J.; Bates, M.; Zhuang, X. Sub-Diffraction-Limit Imaging by Stochastic Optical

        Reconstruction Microscopy (STORM). *Nat. Methods* **2006**, *3* (10), 793–795.

        https://doi.org/10.1038/nmeth929.

(8)   Gwosch, K. C.; Pape, J. K.; Balzarotti, F.; Hoess, P.; Ellenberg, J.; Ries, J.; Hell, S. W.

        MINFLUX Nanoscopy Delivers 3D Multicolor Nanometer Resolution in Cells. *Nat.

        Methods* **2020**, *17* (2), 217–224. https://doi.org/10.1038/s41592-019-0688-0.

(9)   De Boer, P.; Hoogenboom, J. P.; Giepmans, B. N. G. Correlated Light and Electron

        Microscopy: Ultrastructure Lights Up! *Nat. Methods* **2015**, *12* (6), 503–513.

https://doi.org/10.1038/nmeth.3400.

(10) Hauser, M.; Wojcik, M.; Kim, D.; Mahmoudi, M.; Li, W.; Xu, K. Correlative Super-Resolution Microscopy: New Dimensions and New Opportunities. *Chem. Rev.* **2017**, *117* (11), 7428–7456. https://doi.org/10.1021/acs.chemrev.6b00604.

(11) van Elsland, D. M.; Bos, E.; Pawlak, J. B.; Overkleeft, H. S.; Koster, A. J.; van Kasteren, S. I. Correlative Light and Electron Microscopy Reveals Discrepancy between Gold and Fluorescence Labelling. *J. Microsc.* **2017**, *267* (3), 309–317. https://doi.org/10.1111/jmi.12567.

(12) Fukushima, S.; Furukawa, T.; Niioka, H.; Ichimiya, M.; Sannomiya, T.; Tanaka, N.; Onoshima, D.; Yukawa, H.; Baba, Y.; Ashida, M.; Miyake, J.; Araki, T.; Hashimoto, M. Correlative Near-Infrared Light and Cathodoluminescence Microscopy Using Y_2O_3:Ln, Yb (Ln = Tm, Er) Nanophosphors for Multiscale, Multicolour Bioimaging. *Sci. Rep.* **2016**, *6*, 1–11. https://doi.org/10.1038/srep25950.

(13) Niioka, H.; Furukawa, T.; Ichimiya, M.; Ashida, M.; Araki, T.; Hashimoto, M. Multicolor Cathodoluminescence Microscopy for Biological Imaging with Nanophosphors. *Appl. Phys. Express* **2011**, *4* (11), 2–5. https://doi.org/10.1143/APEX.4.112402.

(14) Fukushima, S.; Furukawa, T.; Niioka, H.; Ichimiya, M.; Miyake, J.; Ashida, M.; Araki, T.; Hashimoto, M. Y_2O_3: Tm,Yb Nanophosphors for Correlative Upconversion Luminescence and Cathodoluminescence Imaging. *Micron* **2014**, *67*, 90–95. https://doi.org/10.1016/j.micron.2014.07.002.

(15) Keevend, K.; Stiefel, M.; Neuer, A. L.; Matter, M. T.; Neels, A.; Bertazzo, S.; Herrmann, I. K. Tb^{3+}-Doped LaF_3 Nanocrystals for Correlative Cathodoluminescence Electron

Microscopy Imaging with Nanometric Resolution in Focused Ion Beam-Sectioned

Biological Samples. *Nanoscale* **2017**, *9* (13), 4383–4387.

https://doi.org/10.1039/c6nr09187c.

(16)   Prigozhin, M. B.; Maurer, P. C.; Courtis, A. M.; Liu, N.; Wisser, M. D.; Siefe, C.; Tian,

B.; Chan, E.; Song, G.; Fischer, S.; Aloni, S.; Ogletree, D. F.; Barnard, E. S.; Joubert, L.

M.; Rao, J.; Alivisatos, A. P.; Macfarlane, R. M.; Cohen, B. E.; Cui, Y.; Dionne, J. A.;

Chu, S. Bright Sub-20-nm Cathodoluminescent Nanoprobes for Electron Microscopy.

Nat. Nanotechnol. **2019**, *14* (5), 420–425. https://doi.org/10.1038/s41565-019-0395-0.

(17)   Kimura, E.; Sekiguchi, T.; Oikawa, H.; Niitsuma, J.; Nakayama, Y.; Suzuki, H.; Kimura,

M.; Fujii, K.; Ushiki, T. Cathodoluminescence Imaging for Identifying Uptaken

Flourescence Materials in Kupffer Cells Using Scanning Electron Microscopy. *Archives of

Histology and Cytology*. 2004, pp 263–270. https://doi.org/10.1679/aohc.67.263.

(18)   Furukawa, T.; Niioka, H.; Ichimiya, M.; Nagata, T.; Ashida, M.; Araki, T.; Hashimoto, M.

High-Resolution Microscopy for Biological Specimens via Cathodoluminescence of Eu-

and Zn-Doped Y_2O_3 nanophosphors. *Opt. Express* **2013**, *21* (22), 25655.

https://doi.org/10.1364/oe.21.025655.

(19)   Nagarajan, S.; Pioche-Durieu, C.; Tizei, L. H. G.; Fang, C. Y.; Bertrand, J. R.; Le Cam,

E.; Chang, H. C.; Treussart, F.; Kociak, M. Simultaneous Cathodoluminescence and

Electron Microscopy Cytometry of Cellular Vesicles Labeled with Fluorescent

Nanodiamonds. *Nanoscale* **2016**, *8* (22), 11588–11594.

https://doi.org/10.1039/c6nr01908k.

(20)   Keevend, K.; Coenen, T.; Herrmann, I. K. Correlative Cathodoluminescence Electron

Microscopy Bioimaging: Towards Single Protein Labelling with Ultrastructural Context. *Nanoscale* **2020**, *12* (29), 15588–15603. https://doi.org/10.1039/d0nr02563a.

(21) Egerton, R. F. Mechanisms of Radiation Damage in Beam-Sensitive Specimens, for TEM Accelerating Voltages between 10 and 300 kV. *Microsc. Res. Tech.* **2012**, *75* (11), 1550–1556. https://doi.org/10.1002/jemt.22099.

(22) Giepmans, B. N. G.; Deerinck, T. J.; Smarr, B. L.; Jones, Y. Z.; Ellisman, M. H. Correlated Light and Electron Microscopic Imaging of Multiple Endogenous Proteins Using Quantum Dots. *Nat. Methods* **2005**, *2* (10), 743–749. https://doi.org/10.1038/nmeth791.

(23) Lee, S. F.; Osborne, M. A. Brightening, Blinking, Bluing and Bleaching in the Life of a Quantum Dot: Friend or Foe? *ChemPhysChem* **2009**, *10* (13), 2174–2191. https://doi.org/10.1002/cphc.200900200.

(24) Glenn, D. R.; Zhang, H.; Kasthuri, N.; Schalek, R.; Lo, P. K.; Trifonov, A. S.; Park, H.; Lichtman, J. W.; Walsworth, R. L. Correlative Light and Electron Microscopy Using Cathodoluminescence from Nanoparticles with Distinguishable Colours. *Sci. Rep.* **2012**, *2*, 1–6. https://doi.org/10.1038/srep00865.

(25) Zhong, Y.; Ma, Z.; Wang, F.; Wang, X.; Yang, Y.; Liu, Y.; Zhao, X.; Li, J.; Du, H.; Zhang, M.; Cui, Q.; Zhu, S.; Sun, Q.; Wan, H.; Tian, Y.; Liu, Q.; Wang, W.; Garcia, K. C.; Dai, H. In Vivo Molecular Imaging for Immunotherapy Using Ultra-Bright near-Infrared-IIb Rare-Earth Nanoparticles. *Nat. Biotechnol.* **2019**, *37*, 1322–1331. https://doi.org/10.1038/s41587-019-0262-4.

(26) Jiang, G.; Pichaandi, J.; Johnson, N. J. J.; Burke, R. D.; Van Veggel, F. C. J. M. An

Effective Polymer Cross-Linking Strategy to Obtain Stable Dispersions of Upconverting

$NaYF_4$ Nanoparticles in Buffers and Biological Growth Media for Biolabeling

Applications. *Langmuir* **2012**, *28* (6), 3239–3247. https://doi.org/10.1021/la204020m.

(27) Fischer, S.; Mehlenbacher, R. D.; Lay, A.; Siefe, C.; Alivisatos, A. P.; Dionne, J. A. Small

Alkaline-Earth-Based Core/Shell Nanoparticles for Efficient Upconversion. *Nano Lett.*

2019, *19* (6), 3878–3885. https://doi.org/10.1021/acs.nanolett.9b01057.

(28) Fischer, S.; Siefe, C.; Swearer, D. F.; Claire, M.; Alivisatos, A. P.; Dionne, J. A. Bright

Infrared to Ultraviolet and Visible Upconversion in Small Alkaline Earth-Based

Nanoparticles with Biocompatible CaF_2 Shells. *Angew. Chemie - Int. Ed.* **2020**, *59*,

21603–21612. https://doi.org/10.1002/anie.202007683.

(29) Sun, X.; Wang, B.; Kempson, I.; Liu, C.; Hou, Y.; Gao, M. Restructuring and Remodeling

of $NaREF_4$ Nanocrystals by Electron Irradiation. *Small* **2014**, *10* (22), 4711–4717. https://

doi.org/10.1002/smll.201401101.

(30) Keevend, K.; Puust, L.; Kurvits, K.; Gerken, L. R. H.; Starsich, F. H. L.; Li, J. H.; Matter,

M. T.; Spyrogianni, A.; Sotiriou, G. A.; Stiefel, M.; Herrmann, I. K. Ultrabright and

Stable Luminescent Labels for Correlative Cathodoluminescence Electron Microscopy

Bioimaging. *Nano Lett.* **2019**, *19* (9), 6013–6018.

https://doi.org/10.1021/acs.nanolett.9b01819.

(31) Niitsuma, J. I.; Oikawa, H.; Kimura, E.; Ushiki, T.; Sekiguchi, T. Cathodoluminescence

Investigation of Organic Materials. *J. Electron Microsc.* **2005**, *54* (4), 325–330.

https://doi.org/10.1093/jmicro/dfi043.

(32) Jain, A.; Ong, S. P.; Hautier, G.; Chen, W.; Richards, W. D.; Dacek, S.; Cholia, S.;

Gunter, D.; Skinner, D.; Ceder, G.; Persson, K. A. Commentary: The Materials Project: A Materials Genome Approach to Accelerating Materials Innovation. *APL Mater.* **2013**, *1* (1). https://doi.org/10.1063/1.4812323.

(33)   Kociak, M.; Zagonel, L. F. Cathodoluminescence in the Scanning Transmission Electron Microscope. *Ultramicroscopy* **2017**, *176*, 112–131. https://doi.org/10.1016/j.ultramic.2017.03.014.

(34)   Götze, J. Cathodoluminescence in Applied Geosciences. In *Cathodoluminescence in Geosciences*; Pagel, M., Barbin, V., Blanc, P., Ohnenstetter, D., Eds.; Springer Berlin Heidelberg: Berlin, Heidelberg, 2000; pp 457–477. https://doi.org/10.1007/978-3-662-04086-7_18.

(35)   Wang, Z. L.; Quan, Z. W.; Jia, P. Y.; Lin, C. K.; Luo, Y.; Chen, Y.; Fang, J.; Zhou, W.; O'Connor, C. J.; Lin, J. A Facile Synthesis and Photoluminescent Properties of Redispersible CeF_3, CeF_3:Tb^{3+}, and CeF_3:Tb^{3+}/LaF_3 (Core/Shell) Nanoparticles. *Chem. Mater.* **2006**, *18* (8), 2030–2037. https://doi.org/10.1021/cm052360x.

(36)   Jamalaiah, B. C.; Suresh Kumar, J.; Mohan Babu, A.; Suhasini, T.; Rama Moorthy, L. Photoluminescence Properties of Sm^{3+} in LBTAF Glasses. *J. Lumin.* **2009**, *129* (4), 363–369. https://doi.org/10.1016/j.jlumin.2008.11.001.

(37)   Lai, B.; Feng, L.; Wang, J.; Su, Q. Optical Transition and Upconversion Luminescence in Er^{3+} Doped and Er^{3+}-Yb^{3+} Co-Doped Fluorophosphate Glasses. *Opt. Mater. (Amst).* **2010**, *32* (9), 1154–1160. https://doi.org/10.1016/j.optmat.2010.03.023.

(38)   Ragin, T.; Baranowska, A.; Sołtys, M.; Górny, A.; Zmojda, J.; Kochanowicz, M.; Miluski, P.; Jadach, R.; Dorosz, D. Up-Conversion Luminescence in Low Phonon Heavy Metal

Oxide Glass Co-Doped with Er^{3+}/Ho^{3+} Ions. *Photonics Lett. Pol.* **2018**, *10* (1), 2–4. https://doi.org/10.4302/plp.v10i1.802.

(39)   Nico, C.; Fernandes, R.; Graça, M. P. F.; Elisa, M.; Sava, B. A.; Monteiro, R. C. C.; Rino, L.; Monteiro, T. Eu^{3+} Luminescence in Aluminophosphate Glasses. *J. Lumin.* **2014**, *145*, 582–587. https://doi.org/10.1016/j.jlumin.2013.08.041.

(40)   Zaleta-Alejandre, E.; Zapata-Torres, M.; García-Hipólito, M.; Aguilar-Frutis, M.; Alarcón-Flores, G.; Guzmán-Mendoza, J.; Falcony, C. Structural and Luminescent Properties of Europium Doped TiO_2 Thick Films Synthesized by the Ultrasonic Spray Pyrolysis Technique. *J. Phys. D. Appl. Phys.* **2009**, *42* (9). https://doi.org/10.1088/0022-3727/42/9/095102.

(41)   Yi, G.; Mei, B.; Li, W.; Song, J.; Liu, Z.; Zhou, Z.; Su, L. Synthesis and Luminescence Characterization of Pr^{3+}, Gd^{3+} Co-Doped SrF_2 Transparent Ceramics. *J. Am. Ceram. Soc.* **2020**, *103* (1), 279–286. https://doi.org/10.1111/jace.16728.

(42)   Galloway, S.; Stowe, D.; Vince, R.; Beeching, L.; Blackwell, J. Apparatus for Collection of Cathodoluminescence Signals. 12/309,026, 2013.

(43)   Schefold, J.; Meuret, S.; Schilder, N.; Coenen, T.; Agrawal, H.; Garnett, E. C.; Polman, A. Spatial Resolution of Coherent Cathodoluminescence Super-Resolution Microscopy. *ACS Photonics* **2019**, *6* (4), 1067–1072. https://doi.org/10.1021/acsphotonics.9b00164.

(44)   Zagonel, L. F.; Mazzucco, S.; Tence; March, K.; Bernard, R.; Laslier, B.; Jacopin, G.; Tchernycheva, M.; Rigutti, L.; Julien, F. H.; Songmuang, R.; Kociak, M. Nanometer Scale Spectral Imaging of Quantum Emitters in Nanowires and Its Correlation to Their Atomically Resolved Structure. *Nano Lett.* **2011**, *11* (2), 568–573. https://doi.org/10.1021/

nl103549t.

(45)   Mahfoud, Z.; Dijksman, A. T.; Javaux, C.; Bassoul, P.; Baudrion, A. L.; Plain, J.;
       Dubertret, B.; Kociak, M. Cathodoluminescence in a Scanning Transmission Electron
       Microscope: A Nanometer-Scale Counterpart of Photoluminescence for the Study of II-VI
       Quantum Dots. *J. Phys. Chem. Lett.* **2013**, *4* (23), 4090–4094.
       https://doi.org/10.1021/jz402233x.

(46)   Jacobsohn, L. G.; Sprinkle, K. B.; Roberts, S. A.; Kucera, C. J.; James, T. L.; Yukihara, E.
       G.; Devol, T. A.; Ballato, J. Fluoride Nanoscintillators. *J. Nanomater.* **2011**, *2011*. https://
       doi.org/10.1155/2011/523638.

(47)   Moore, D. T.; Berger, B. W.; DeGrado, W. F. Protein-Protein Interactions in the
       Membrane: Sequence, Structural, and Biological Motifs. *Structure* **2008**, *16* (7), 991–
       1001. https://doi.org/10.1016/j.str.2008.05.007.Protein-Protein.

(48)   Yang, X.; Hou, D.; Jiang, W.; Zhang, C. Intercellular Protein-Protein Interactions at
       Synapses. *Protein Cell* **2014**, *5* (6), 420–444. https://doi.org/10.1007/s13238-014-0054-z.

(49)   Zagonel, L. F.; Rigutti, L.; Tchernycheva, M.; Jacopin, G.; Songmuang, R.; Kociak, M.
       Visualizing Highly Localized Luminescence in GaN/AlN Heterostructures in Nanowires.
       Nanotechnology **2012**, *23* (45). https://doi.org/10.1088/0957-4484/23/45/455205.

(50)   Pennycook, S. J.; Howie, A. Study of Single-Electron Excitations by Electron Microscopy
       II. Cathodoluminescence Image Contrast from Localized Energy Transfers. *Philos. Mag.
       A Phys. Condens. Matter, Struct. Defects Mech. Prop.* **1980**, *41* (6), 809–827.
       https://doi.org/10.1080/01418618008243890.

(51)   Yacobi, B. G.; Holt, D. B. Cathodoluminescence Scanning Electron Microscopy of

Semiconductors. *J. Appl. Phys.* **1986**, *59* (4), R1–R24.

https://doi.org/https://doi.org/10.1063/1.336491.

(52)   Muto, S.; Shiga, M. Application of Machine Learning Techniques to Electron

Microscopic/Spectroscopic Image Data Analysis. *Microscopy* **2020**, *69* (2), 110–122.

https://doi.org/10.1093/jmicro/dfz036.

TOC Figure: